

Optical phonons in spherical core/shell semiconductor nanoparticles: Effect of hydrostatic pressure

C. Trallero-Giner,¹ F. Comas,² G. E. Marques,³ R. E. Tallman,⁴ and B. A. Weinstein⁴

¹*Department of Theoretical Physics, Havana University, Havana 10400, Cuba*

²*Department of Natural and Social Sciences, Miami Dade College, Interamerican Campus, Miami, Florida 33135, USA*

³*Departamento de Física, Universidade Federal de São Carlos, 13565-905 São Carlos, SP, Brazil*

⁴*Department of Physics, SUNY at Buffalo, 239 Fronczak Hall, Buffalo, New York 14260-1500, USA*

(Received 18 May 2010; revised manuscript received 15 August 2010; published 17 November 2010)

By applying a phenomenological macroscopic approach we have studied polar optical phonons in core-shell semiconductor hybrid nanoparticles with spherical shape. The coupling of electromechanical oscillations is taken into account within the long-wavelength limit. A detailed analysis of the optical-phonon modes is presented with emphasis on the phonon-dispersion laws. Different kinds of II-VI and III-V semiconductor compounds are discussed, showing the differences resulting from their bulk phonon frequency dependence on the wave vector, and on the shell-to-core radius ratio. We make a systematic application of the theory for different nanostructures and report all possible polar optical-phonon modes. The effects of hydrostatic pressure on confined and surface-optical-phonon mode optical vibrations are considered. Also, we provide results for the usual dielectric continuum approach as a function of the applied pressure, where just the electric aspect of the oscillations is addressed. The effects of pressure on confined LO- and TO-like, and on surface-optical-phonon modes in core/shell InP/CdS nanoparticles are explored by Raman scattering. The observed pressure-induced shifts of the Raman spectra are well described by the theoretical calculations, and by applying a fitting procedure to the data we may extract the value for the core diameter and the shell-to-core radius ratio.

DOI: [10.1103/PhysRevB.82.205426](https://doi.org/10.1103/PhysRevB.82.205426)

PACS number(s): 78.67.Bf, 68.65.Hb, 63.22.-m

I. INTRODUCTION

Colloidal chemistry methods, with an appropriate handling of the reaction kinetics, have allowed the growth of core-shell quantum-dot (QD) semiconductor nanostructures. This method enables one to obtain semiconductor nanostructures in the form of dots, tubes, wires, etc., with a relatively high control of their sizes and shapes and displaying rather interesting optic and electronic size-dependent properties.¹⁻⁷ Based on several types of III-V and II-VI materials, hybrid core-shell nanoparticles have been synthesized, showing unique physical properties and promising perspectives for the development of novel devices.⁸⁻¹⁴ In these systems, a few monolayers of material “2” are grown on a core structure of material “1” and, after which the whole system is embedded in a host material, that may be a silicate matrix or an organic polymeric compound.

In the current work we are essentially concerned with polar optical-phonon properties. Usually and for simplicity, the so-called dielectric continuum approach (DCA) is applied for a theoretical estimation of the confined TO and LO bulklike phonon frequencies, while, in the case of small-size crystal heterostructures, the interface phonons also should be included.¹⁵ Most of the theoretical studies have considered the spherical geometry¹⁵⁻¹⁹ while Refs. 20 and 21 treats spheroidal geometry QDs. A more reliable phenomenological macroscopic approach (PMA), providing results beyond the DCA, was developed in Refs. 22-25. In contrast with the strictly electric character of the DCA, the PMA treatment for polar optical phonons takes into account the coupled electro-mechanical character of the vibrations. Application of the correct matching boundary conditions at the heterostructure interfaces for both the electrical and mechanical quantities

leads to the mixing of the different phonon modes. Modes of mixed nature are indeed obtained and may display predominant LO, TO, or interface profiles in different regions of the vibrational spectra. The general trend of this PMA for optical vibrations in nanostructures has been discussed in several previous references and we shall not give here a detailed description of the method²²⁻²⁵ but focus on the generalization of the phonon model to hybrid core-shell nanoparticles under pressure (P). We shall consider three possible core-shell hybrid nanoparticles: CdSe/CdS, CdS/HgS, and InP/CdS. In the framework of the present paper we make a detailed analysis of the consequences of the general curvature in the bulk phonon-dispersion curves for the possible optical vibrational modes, after a systematic application of the PMA described in the above-mentioned references.

From the point of view of the vibrational spectra of hybrid nanoparticles, the material 1 shows a true quantum-dot behavior for the polar optical oscillations, while inside the layer of material 2, the system actually represents a quantum-well structure for the phonon modes. Raman spectroscopy can be employed to detect these different aspects in the phonon modes of hybrid nanoparticles.^{26,27} Moreover, pressure-Raman studies can be an important tool for the understanding of vibrational modes, identifying confined and surface modes, helping to determine the core radius and shell-core size ratio, and providing information on the shape and stability of semiconductor nanoparticles (see, for example, Refs. 28-33). Measurements of the effects of applied pressure on the Raman spectrum of InP/CdS nanoparticles were carried out and given preliminary interpretation by Tallman *et al.*²⁷ Here, these experimental results are employed to test the generalized PMA model developed for hybrid nanoparticles in the present work, particularly the model's detailed

predictions for the dispersion relations of the confined and surface-optical (SO) modes as functions of the applied pressure and the core-shell dimensions. It is found that the spectral tuning achieved in high-pressure Raman experiments permits one, not only to test theoretical macroscopic models, but also to extract important information on as-grown conditions and on geometrical dimensions in these novel semiconductor nanostructures.

We organized the paper as follows. In Sec. II we briefly summarize the fundamental equations used in this work and the description of our model system. Section III is dedicated to the essential analytical results for the core modes, shell modes, and interface phonons of nanoparticles with spherical symmetry. In Sec. IV we present the specific calculations at $P=0$ for several hybrid nanostructures obtaining the dispersion of core and shell modes as a function of the shell-to-core radii ratio, and discussing the physical interpretation of the main results. Also, we present the dependence of the interface phonons on the core/shell geometry and on the external hydrostatic pressure. Section V compares the theoretical and experimental results for the effects of applied hydrostatic pressure on the Raman spectra of InP/CdS hybrid nanoparticles. From the analysis of the phonon frequencies corresponding to different angular momenta, core radii and shell-to-core radii ratio, we are able to obtain a satisfactory fit of the observed pressure dependence of the confined LO and TO modes, and the surface phonons to the theoretically predicted behavior under applied pressure. Finally, in Sec. VI we present our conclusions.

II. THEORETICAL BACKGROUND

In the present work the PMA formalism is extended to calculate the effects of applied pressure on the optical-phonon modes of spherical core-shell nanoparticles. The fundamental equations describing our treatment of the optical phonons as function of pressure (P) can be cast in the form²²⁻²⁵

$$[\omega^2 - \omega_T^2(P)]\mathbf{u} = \frac{\alpha(P)}{\rho(P)} \nabla \varphi + \beta_L^2 \nabla \nabla \cdot \mathbf{u} - \beta_T^2 \nabla \times \nabla \times \mathbf{u} \quad (1)$$

and

$$\nabla^2 \varphi = \frac{4\pi\alpha(P)}{\epsilon_\infty(P)} \nabla \cdot \mathbf{u} \quad (2)$$

with

$$\alpha^2(P) = \frac{\epsilon_0(P) - \epsilon_\infty(P)}{4\pi} \rho(P) \omega_T^2(P). \quad (3)$$

In the above equations ρ is the reduced mass density, ω_T (ω_L) is the transversal (longitudinal) bulk semiconductor limiting frequency at the Γ point of the Brillouin zone, and ϵ_0 (ϵ_∞) is the static (high-frequency) dielectric constant. The relative mechanical displacement of the ions (in units of length) is represented by \mathbf{u} , φ is the electric potential due to the polar character of the vibrations, the term α takes into account the

coupling between the mechanical field and electrostatic field, and the parameter β_T (β_L) is introduced in order to describe the quadratic curvature of the TO (LO)-bulk phonon band, which is assumed to be pressure independent.³⁴ We also assume that the Lyddane-Sachs-Teller relation $\omega_L^2(P) = \omega_T^2(P) \epsilon_0(P) / \epsilon_\infty(P)$ holds. Maxwell's equations are treated in the quasistationary approximation and the harmonic time dependence $f(t) \sim \exp(-i\omega t)$ is assumed to be valid for all the involved quantities.

Concerning Eqs. (1) and (2), it is possible to prove that their solutions for the bulk semiconductor case lead to TO and LO phonons with the frequencies $\omega^2(P) = \omega_T^2(P) - \beta_T^2 \kappa^2$ and $\omega^2(P) = \omega_L^2(P) - \beta_L^2 \kappa^2$, respectively. With an appropriate fitting of the parameters β_L and β_T we may adjust to the reported dispersion laws of the bulk semiconductors, providing we limit ourselves to a region not too far from the Γ point. However, it should be realized that some of the more commonly used semiconductor compounds show increasing frequency for increasing κ . For such a situation we need to change the sign of the second term on the right-hand side of the dispersion law, an issue which can be easily achieved with the formal substitutions $\beta_T \rightarrow i\beta_T$ and $\beta_L \rightarrow i\beta_L$ (where $i = \sqrt{-1}$). Of course this change must be done in the fundamental Eq. (1) whenever a bulk semiconductor having this kind of polar optical-phonon-dispersion law is involved.

For systems of finite dimensions the solutions of Eqs. (1) and (2) must meet adequate boundary conditions at the interface S . The electric potential φ , as usual, should be continuous at the interface as well as the normal component of the electric induction vector \mathbf{D} , which, according to the employed theory, is expressed by: $\mathbf{D} = 4\pi\alpha(P)\mathbf{u} - \epsilon_\infty(P)\nabla\varphi$. The other boundary conditions are related to the displacement vector field \mathbf{u} . In the usual case we must require continuity of the vector \mathbf{u} at S and also continuity of the normal component of the force flux (as occurs in the case of any ordinary elastic medium).²²⁻²⁵ However, within the limits of the current work, we adopt the boundary condition of mechanical confinement of the form $\mathbf{u}|_S = 0$. Whenever the mechanical vibrations of one of the materials do not show significant penetration into the other one, the above boundary condition should hold true, a situation met when the fundamental frequency gap between the two semiconductors involved at the interface is large enough.³⁵ Under this approximation, the continuity of the normal component of the induction vector \mathbf{D} at the interface is cast as

$$\epsilon_\infty^<(P) \frac{\partial \varphi^<}{\partial n} \Big|_S = \epsilon_\infty^>(P) \frac{\partial \varphi^>}{\partial n} \Big|_S. \quad (4)$$

In Eq. (4) the symbol $<(>)$ indicates that the associated quantity is taken at the left-hand (right-hand) side of the corresponding interface.

Let us briefly summarize how the analytical solutions of Eqs. (1) and (2) may be achieved. We first define the quantities

$$\Lambda = \nabla \cdot \mathbf{u} \quad \text{and} \quad \Gamma = \nabla \times \mathbf{u}. \quad (5)$$

After substitution of Eq. (5) in Eqs. (1) and (2), we are led to

$$\nabla^2 \Lambda + q^2 \Lambda = 0 \quad \text{with} \quad q^2 = \frac{\omega_L^2(P) - \omega^2}{\beta_L^2}, \quad (6)$$

$$\nabla^2 \Gamma + Q^2 \Gamma = 0 \quad \text{with} \quad Q^2 = \frac{\omega_T^2(P) - \omega^2}{\beta_T^2}. \quad (7)$$

We must notice that the sign of q^2 and/or Q^2 changes if we need to make the formal changes $\beta_{L(T)} \rightarrow i\beta_{L(T)}$ (depending on the type of semiconductor considered, as discussed above).

It is not difficult to prove that the solution of Eq. (2) can be given in the form

$$\varphi = \varphi_h - \frac{4\pi\alpha(P)}{\epsilon_\infty(P)q^2} \Lambda, \quad \text{where} \quad \nabla^2 \varphi_h = 0. \quad (8)$$

On the other hand, the general solution for \mathbf{u} may be expressed as follows:

$$\mathbf{u} = -\frac{\alpha(P)}{\rho(P)\beta_T^2 Q^2} \nabla \varphi_h - \frac{1}{q^2} \nabla \Lambda + \frac{1}{Q^2} \nabla \times \Gamma. \quad (9)$$

As seen from Eqs. (8) and (9), the needed quantities are φ_h , Λ , and Γ (actually we just need the curl of Γ), such that the required boundary conditions can be fulfilled. Concerning φ and Λ we must solve the Laplace and Helmholtz equations but in the case of Eq. (7) the vector $\Gamma = \mathbf{M} + \mathbf{N}$ with

$$\mathbf{M} = \nabla \times (v^{(1)} \mathbf{r}) \quad \text{and} \quad \mathbf{N} = \frac{1}{Q} \nabla \times \nabla \times (v^{(2)} \mathbf{r}), \quad (10)$$

and $v^{(i)}$ ($i=1,2$) are solutions of the scalar equation $\nabla^2 v^{(i)} + Q^2 v^{(i)} = 0$ (see Refs. 22 and 36).

In order to proceed further, the geometry and fundamental properties of the physical system considered should be established. Concerning the quantities q^2 and Q^2 , they can be positive or negative depending on the frequency interval in-

olved. For instance, if the expression for Q^2 , given in Eq. (7), has a positive β_T^2 term, then $Q^2 > 0$ ($Q^2 < 0$) for $\omega < \omega_T$ ($\omega > \omega_T$). For a semiconductor compound such that $\beta_T^2 < 0$ the converse conditions are met. Since we are assuming here the spherical geometry, as done in Ref. 22, we may make use of some of the essential results reported in that reference.

III. SOLUTION OF THE PMA EQUATIONS FOR SPHERICAL HYBRID NANOPARTICLES

In the previous section we have summarized the fundamental equations that we must handle in our treatment of the PMA and also the general method that we apply for finding their analytical solutions. Let us now focus on the concrete system we are interested to study, namely, a spherical hybrid nanostructure modeled as follows: using spherical coordinates (r, θ, ϕ) in the interval $r < a$ ($a < r < b$) we have a semiconductor labeled as 1 (semiconductor labeled as 2) and for $r > b$ a host material is assumed in the form of an infinite dielectric medium which does not take part in the oscillations and is described through its dielectric constant $\epsilon_D(P)$. Then, within the chosen model system we have two spherical interfaces at $r=a$ and $r=b$. The analysis of the solutions using the spherical symmetry of our model system must be considered in two parts.

A. Core modes

We consider $\mathbf{u} \equiv 0$ for $a < r < b$ but $\mathbf{u} \neq 0$ for $r < a$. In this case we need Λ just for $r < a$ and it is easy to see that $\Lambda \sim j_l(qr)Y_{lm}(\theta, \phi)$, where $j_l(x)$ are spherical Bessel functions and $Y_{lm}(\theta, \phi)$ are spherical harmonics.³⁷ The electric potential is obtained from Eq. (8) and given in the form

$$\varphi(\mathbf{r}) = Y_{lm}(\theta, \phi) \begin{cases} A^{(1)} \left[\frac{r}{a(P)} \right]^l - \frac{4\pi\alpha_1(P)a^2(P)}{\epsilon_{1\infty}(P)v_1^2} A^{(2)} j_l(q_1 r) & r < a(P), \\ A^{(3)} \left[\frac{r}{a(P)} \right]^l + \left[A^{(1)} - A^{(3)} - \frac{4\pi\alpha_1(P)a^2(P)}{\epsilon_{1\infty}(P)v_1^2} j_l(v_1) A^{(2)} \right] \left[\frac{a(P)}{r} \right]^{l+1} & a(P) < r < b(P), \\ \left[A^{(1)} + [\gamma(P)^{2l+1} - 1] A^{(3)} - \frac{4\pi\alpha_1(P)a^2(P)}{\epsilon_{1\infty}(P)v_1^2} j_l(v_1) A^{(2)} \right] \left[\frac{a(P)}{r} \right]^{l+1} & r > b(P). \end{cases} \quad (11)$$

In Eq. (11) we are using the following notations: $\gamma(P) = b(P)/a(P)$ and $v_1 = q_1 a(P)$. Subscripts 1 or 2 attached to a given physical quantity indicates the two possible semiconductor compounds involved. The potential φ is already continuous at the interfaces [$r=a(P)$ and $r=b(P)$] and there appear three constants ($A^{(i)}$, $i=1,2,3$) to be determined by the matching boundary conditions. We should keep in mind that $q^2 = \pm [\omega_L^2(P) - \omega^2]/\beta_L^2$ depending on the type of semicon-

ductor involved. In any case q remains a real quantity due to the values taken by the frequency ω .

The general solution for the scalar functions $v^{(i)}(\mathbf{r})$ can be chosen as

$$v^{(i)}(\mathbf{r}) = Y_{lm}(\theta, \phi) w_l^{(i)}(Q_i r). \quad (12)$$

According to Eq. (10) we obtain that $\nabla \times \Gamma = \nabla \times M + \nabla \times N$, where

$$\nabla \times M = \frac{l(l+1)}{r} w_l^{(1)}(Q_1 r) Y_{lm} \mathbf{e}_r - \frac{i\sqrt{l(l+1)}}{r} \frac{d}{dr} [r w_l^{(1)}(Q_1 r)] \mathbf{e}_r \times \mathbf{X}_{lm} \quad (13)$$

and

$$\nabla \times N = i\sqrt{l(l+1)} w_l^{(2)}(Q_1 r) \mathbf{X}_{lm}. \quad (14)$$

For the case of the core, where $0 < r < a$ the bounded solutions for $w_l^{(i)}$ are

$$w_l^{(i)} = \begin{cases} j_l(Q_1 r) & Q^2 > 0 \\ i_l(Q_1 r) & Q^2 < 0 \end{cases}$$

with $j_l(z)$ [$i_l(z)$] the spherical (modified) Bessel function.

The solutions for the displacement vector \mathbf{u} in the present case differ from zero just for $r < a(P)$ and are given by²²

$$\mathbf{u} = u_r Y_{lm} \mathbf{e}_r + u_T \mathbf{X}_{lm} + u_{L-T} \mathbf{e}_r \times \mathbf{X}_{lm}, \quad (15)$$

where

$$\mathbf{X}_{lm} = \frac{i\sqrt{l(l+1)}}{(2l+1)\sin\theta} \left[\frac{im(2l+1)}{l(l+1)} Y_{lm} \mathbf{e}_\theta + \left(-\sqrt{\frac{(2l+1)(l+m+1)}{(2l+3)(l-m+1)}} \frac{l-m+1}{l+1} Y_{l+1,m} + \sqrt{\frac{(2l+1)(l-m)}{(2l-1)(l+m)}} \frac{l+m}{l} Y_{l-1,m} \right) \mathbf{e}_\phi \right]. \quad (16)$$

In Eqs. (13)–(16) \mathbf{e}_r , \mathbf{e}_θ , and \mathbf{e}_ϕ are the unit vectors for the spherical coordinates. It must be remarked that the expression for \mathbf{X}_{lm} has an erratum in Ref. 22 which has been corrected here. By a straightforward application of the above equations we get for $r < a(P)$,

$$u_r = \left\{ -A^{(1)} \frac{l\alpha_1(P)a(P)}{\rho_1(P)\beta_{1T}^2\mu_1^2} \left[\frac{r}{a(P)} \right]^{l-1} - A^{(2)} \frac{a(P)}{\nu_1} j_l'(q_1 r) + A^{(4)} \frac{l(l+1)a(P)}{\mu_1^2} \frac{a(P)}{r} j_l(Q_1 r) \right\}, \quad (17)$$

$$u_T = -iB \frac{\sqrt{l(l+1)}}{Q_1} j_l(Q_1 r), \quad (18)$$

$$u_{L-T} = i\sqrt{l(l+1)} \left\{ A^{(1)} \frac{\alpha_1(P)a(P)}{\rho_1(P)\beta_{1T}^2\mu_1^2} \left[\frac{r}{a(P)} \right]^{l-1} + A^{(2)} \frac{a(P)}{\nu_1^2} \frac{a(P)}{r} j_l(q_1 r) - A^{(4)} \frac{a(P)}{\mu_1^2} \frac{a(P)}{r} [j_l(Q_1 r) + Q_1 r j_l'(Q_1 r)] \right\}. \quad (19)$$

In the latter set of equations $A^{(4)}$ and B are constants, the prime on the function $j_l(z)$ denotes the first derivative with respect to the argument and $\mu_1 = Q_1 a(P)$. For $Q_1^2 < 0$ the spherical Bessel function $j_l(z)$ should be replaced by the modified Bessel function $i_l(z)$.³⁷ It must be noticed that the component u_T represents uncoupled transversal mechanical oscillations of semiconductor 1 [for $r < a(P)$], which were

already studied in Ref. 38. On the other hand, the components u_r and u_{L-T} are coupled oscillations, which are also coupled to the scalar potential φ . It should be realized that the angular dependence of the components labeled by “ r ,” “ T ,” and “ $L-T$ ” actually are given through Y_{lm} , and the vectors \mathbf{X}_{lm} and $\mathbf{e}_r \times \mathbf{X}_{lm}$, respectively.

Applying the matching boundary condition (4) to the electrostatic potential $\varphi(r, \theta, \phi)$ given in Eq. (11) at $r = a(P)$ and $r = b(P)$, and also the conditions $u_r|_a = 0$ and $u_{L-T}|_a = 0$ provide us with the secular equation

$$\nu_1 j_l'(\nu_1) F_l(\mu_1; P) = l(l+1) j_l(\nu_1) G_l(\mu_1; P), \quad (20)$$

where the functions $F_l(\mu; P)$ and $G_l(\mu; P)$ are given in Appendix A. We can also verify that

$$\beta_{1L}^2 \nu_1^2 - \beta_{1T}^2 \mu_1^2 = [\omega_L^2(P) - \omega_T^2(P)] a^2(P), \quad (21)$$

making it clear that parameters μ_1 and ν_1 are not independent quantities. Let us recall once more that, whenever the parameter μ_1 becomes a pure imaginary quantity the Bessel function $j_l(\mu_1)$ should be replaced by the modified Bessel function $i_l(\mu_1)$. On the other hand, Eq. (21) is valid for $\beta_L^2 > 0$ and $\beta_T^2 > 0$. Otherwise, depending on the κ dependence of the bulk phonon modes in the analyzed semiconductor compound, we should perform the changes already discussed in Sec. II.

Equation (20) determines the core optical phonon dispersion law as a function of the core and shell dimensions for the spherical hybrid nanoparticles. This is formally analogous to the one reported in Ref. 22, as may be expected, but now the functions $F_l(\mu; P)$ and $G_l(\mu; P)$ are somewhat different. Solving the transcendental Eq. (20) we can find, for each value of $l=0, 1, 2, \dots$, the phonon frequencies as a function of P and $\gamma(P)$. Hence, the set of frequencies $\omega_{l,N}(P)$ depends on the nanostructure through the ratio $\gamma(P) = b(P)/a(P)$.

For $l=0$ we obtain from Eq. (20) pure core-confined uncoupled phonons having (a) LO character and frequencies as functions of P given by

$$\omega_{L,l=0,N}^2(P) = \omega_L^2(P) - \frac{\nu_{1,N}^2}{a^2(P)} \beta_{1L}^2, \quad N = 1, 2, \dots, \quad (22)$$

where $\nu_{1,N}$ are the solution of the equation $\tan(z) = z$, and having (b) TO character with

$$\omega_{T,l=0,N}^2(P) = \omega_T^2(P) - \frac{(2N+1)^2 \pi^2}{4a^2(P)} \beta_{1T}^2, \quad N = 0, 1, 2, \dots \quad (23)$$

Notice, that in this case the LO and TO frequencies are independent of the shell width $b(P)$. A compact analytical expression for $l=1$ is displayed in Appendix A.

In the limit $\gamma(P) \rightarrow 1$ [or equivalently $\gamma(P) \rightarrow \infty$] and under the condition $\epsilon_D(P) \rightarrow \epsilon_{\infty}(P)$, Eq. (20) reduces to the case of a single sphere. The main point here is that the region for $r > a(P)$ is now a composite in contrast with the situation considered in Ref. 22 at $P=0$.

B. Shell modes

Here we must consider $\mathbf{u} \equiv 0$ for $r < a(P)$ but $\mathbf{u} \neq 0$ for $a(P) < r < b(P)$. In that case $\Lambda \sim [C_1 j_l(qr) + C_2 n_l(qr)]$

$$\varphi(\mathbf{r}) = Y_{lm}(\theta, \phi) \begin{cases} \left\{ B^{(1)} + B^{(2)} - \frac{1}{v_2^2} [B^{(3)} j_l(v_2) - B^{(4)} n_l(v_2)] \right\} \left[\frac{r}{a(P)} \right]^l & r < a(P), \\ B^{(1)} \left[\frac{r}{a(P)} \right]^l + B^{(2)} \left[\frac{a(P)}{r} \right]^{l+1} - \frac{[B^{(3)} j_l(q_2 r) + B^{(4)} n_l(q_2 r)]}{v_2^2} & a(P) < r < b(P), \\ \left(B^{(1)} \gamma^{2l+1}(P) + B^{(2)} - \frac{\gamma^{l+1}(P)}{v_2^2} \{ B^{(3)} j_l[\gamma(P) v_2] + B^{(4)} n_l[\gamma(P) v_2] \} \right) \left[\frac{a(P)}{r} \right]^{l+1} & r > b(P). \end{cases} \quad (24)$$

As previously, the potential φ is already continuous at $r = a(P)$ and $r = b(P)$ but now involves the four constants B_i ($i = 1, 2, 3, 4$). Let us now summarize the expressions for the components of the vector \mathbf{u} ,

$$u_r = -\frac{\alpha_2(P) a^2(P)}{\rho_2(P) \beta_{2T}^2 \mu_2^2} \left\{ l B^{(1)} \left[\frac{r}{a(P)} \right]^{l-1} - (l+1) B^{(2)} \left[\frac{a(P)}{r} \right]^{l+2} \right\} - \frac{a^2(P)}{v_2} [B^{(3)} j_l'(q_2 r) + B^{(4)} n_l'(q_2 r)] + \frac{l(l+1) a^2(P) a(P)}{\mu_2^2 r} v_l(Q_2 r), \quad (25)$$

$$u_T = -i \frac{\sqrt{l(l+1)}}{Q_2} w_l(Q_2 r), \quad (26)$$

$$u_{L-T} = i \sqrt{l(l+1)} \left(\frac{\alpha_2(P) a^2(P)}{\rho_2(P) \beta_{2T}^2 \mu_2^2} \left\{ B^{(1)} \left[\frac{r}{a(P)} \right]^{l-1} + B^{(2)} \times \left[\frac{a(P)}{r} \right]^{l+2} \right\} + \frac{a^2(P) a(P)}{v_2^2 r} [B^{(3)} j_l(q_2 r) + B^{(4)} n_l(q_2 r)] - \frac{a^2(P) a(P)}{\mu_2^2 r} \frac{d}{dr} [r v_l(Q_2 r)] \right) \quad (27)$$

with

$$v_l(Q_2 r) = B^{(5)} j_l(Q_2 r) + B^{(6)} n_l(Q_2 r) \quad (28)$$

and the function $w_l(Q_2 r)$ is formally analogous to $v_l(Q_2 r)$ but involving different constants. In order to be consistent with the constants appearing in Eq. (24), we define $B^{(i)}/B^{(i)} = \epsilon_{2\infty}(P)/[4\pi\alpha_2(P)a^2(P)]$ for $i = 3, 4, 5, 6$. As in the former case, u_T describes uncoupled transversal oscillations not involving an electric potential, while u_r and u_{L-T} describe the coupled oscillations where the electric potential is also involved. The uncoupled oscillations will not be considered in the present work since they have been previously studied in Ref. 38.

Applying the previously above discussed matching boundary conditions at the interfaces $r = a(P)$ and $r = b(P)$ we

$Y_{lm}(\theta, \phi)$ for $a(P) < r < b(P)$ with $n_l(x)$ the spherical Bessel function of the second kind.^{36,37} Hence, the potential now reads

are able to obtain the phonon frequencies as a function of the parameters γ and P for the different modes in the slab. In Appendix B we have written a simplified expression for the secular determinant, which can be used in the calculations of the shell phonon frequencies $\omega_{l,N}[P, \gamma(P)]$. As in the case of the core modes, for $l=0$ we obtain from Eqs. (B1)–(B6) of Appendix B pure shell-confined uncoupled phonons. For the LO-type modes, the eigensolutions $v_{2,N} = a(P)q_2$ are given by

$$\tan(v_2[\gamma(P) - 1]) = \frac{v_2[\gamma(P) - 1]}{1 + v_2^2 \gamma(P)}. \quad (29)$$

Similarly, for the TO modes we obtain

$$\mu_{2,N} = a(P)Q_2 = \frac{N\pi}{1 - \gamma(P)}, \quad N = 1, 2, \dots \quad (30)$$

Notice that in the case of quantum wells the phonon frequencies would depend on the well width d [in our case $d = b(P) - a(P)$] while for the shell modes the eigenvalues found here depend on the ratio $\gamma(P) = b(P)/a(P)$.

C. Interface phonons

By keeping both the mechanical and the electrostatic fields, coupled via the differential Eqs. (1) and (2), we are led (for $l > 0$) to a general formulation that describes the phonon modes having mixed mechanical and electrical nature.³⁹ The coupled oscillations involve 4×4 and 6×6 systems of linear homogeneous equations which determine the dispersion law for the core and shell modes as a function of P and the ratio $b(P)/a(P)$, respectively. Typically, Raman spectra in hybrid nanoparticles³³ exhibit structures which are related to SO phonons of predominantly electric character. To characterize the pressure-dependent frequencies of these phonons we can use a simplified version of the set of Eqs. (A1) and (B7) given in Appendices A and B. The corresponding SO-phonon frequencies then can be obtained in the framework of the DCA. This model predicts correctly the SO oscillations if the bulk phonon wavelength λ_p is smaller than the characteristic quantum-dot dimension L ($\lambda_p < L$).⁴⁰ In the opposite case where $\lambda_p \geq L$, the preceding more general and complete

approach should be employed in order to obtain a reliable description of optical modes (optical vibron modes⁴¹). Extending the work of Ref. 40 to evaluate the effects of applied

pressure on the SO modes of spherical core-shell nanoparticles within a DCA treatment, we obtain that the corresponding phonon frequencies are given by the equation

$$\frac{\epsilon^{(2)}(\omega, P)}{\epsilon_D(P)} = - \frac{[\gamma^{2l+1}(P) - 1]\epsilon^{(1)}(\omega, P) + \left[1 + \frac{l+1}{l}\gamma^{2l+1}(P)\right]\epsilon^{(2)}(\omega, P)}{[\gamma^{2l+1}(P) - 1]\epsilon^{(2)}(\omega, P) + \left[1 + \frac{l}{l+1}\gamma^{2l+1}(P)\right]\epsilon^{(1)}(\omega, P)} \quad (31)$$

with

$$\epsilon^{(i)}(\omega, P) = \epsilon_{i\infty}(P) \frac{\omega^2 - \omega_{iL}^2(P)}{\omega^2 - \omega_{iT}^2(P)} \quad (32)$$

the dielectric functions for the core ($i=1$) and shell ($i=2$).

Equation (31) provides the SO-phonon frequencies ω_l as a function of the geometric factor $b(P)/a(P)$ and P for different values of angular momentum $l=1, 2, \dots$. The physical nature of these SO-phonon modes is associated with the spatial symmetry of the core-shell structure. For each value of l we have three independent interface optical phonons. One of them is related to the interface phonons of a spherical dot embedded in a host material characterized by a certain effective dielectric constant and the others are connected to the two interfaces involved in the shell structure, i.e., to the case of interface LO phonons of the spherical shell sandwiched between the spherical core and a host dielectric medium. As we stated below, these geometrical properties of the SO phonons can be used to extract quantitative information from Raman measurements about the geometric parameters characterizing the hybrid nanoparticles.

IV. DISPERSION RELATIONS FOR SEVERAL HYBRID NANOPARTICLES

In order to provide deeper understanding of the physical meaning embraced in the equations developed in the previ-

TABLE I. Values of the semiconductor physical parameters.

Parameters	CdS ^a	HgS ^b	CdSe ^c
ϵ_0	8.7 ^d	18.2	9.53
ϵ_∞	5.3	11.36	5.72
ω_L (cm ⁻¹)	305	250 ^e	213.1
ω_T (cm ⁻¹)	238	175 ^e	165.2
β_T (ms ⁻¹ × 10 ³)	1.58	5.25 ^e	0.002
β_L (ms ⁻¹ × 10 ³)	5.04	2.50 ^e	2.969

^aReference 42.

^bReference 43.

^cReference 44.

^dReference 45.

^eReference 46.

ous section we shall discuss the dispersion relations at $P=0$, i.e., the frequency dependence on $\gamma=b/a$, for various optical-phonon modes, considering several core/shell heterostructures made of different II-VI semiconductor compounds. We analyzed two possible hybrid nanostructures: CdSe/CdS and CdS/HgS, discussing their frequency dispersion laws for $l=0$ and 1. The physical parameters of these semiconductor compounds are given in Table I.⁴⁷ Note also that, the bulk semiconductor frequency dependence on the wave vector κ for these materials displays different characters, as may be seen from Table II. The materials for the various core/shell nanostructures were chosen in order to analyze all the possible cases.

In Figs. 1 and 2 we plot the frequency ω for two considered hybrid nanoparticles as a function of the ratio $\gamma=b/a$ and for angular momentum $l=0$. We are showing both the core modes (left panels) related to a sphere ($r<a$) and the shell modes related to a spheroidal slab (right panels) ($a<r<b$). For the $l=0$ symmetry, all modes are uncoupled phonons with purely mechanical nature. For the core region, Eq. (22) leads to longitudinal modes while the transversal modes are given by Eq. (23). In both cases the frequencies do not depend on the ratio γ , but only on the core radius, and therefore they are described by horizontal lines in Figs. 1 and 2. However, the frequency separation between two core modes depends on the core radius a and on the magnitude of the parameter $\beta_{T(L)}$. For the slab region Eq. (29) leads to the roots ν_2 for the longitudinal modes, whereas μ_2 , given by Eq. (30), describes the transversal-optical oscillations. As may be seen, for the shell modes these frequencies depend

TABLE II. Trends for the dependence of the bulk phonon frequencies on wave vector κ .

Material	Longitudinal	Transversal
CdS ^a	Decreasing	Increasing
HgS ^b	Increasing	Increasing
CdSe ^c	Decreasing	Decreasing
InP ^d	Decreasing	Increasing

^aReference 42.

^bReference 43.

^cReference 44.

^dReference 48.

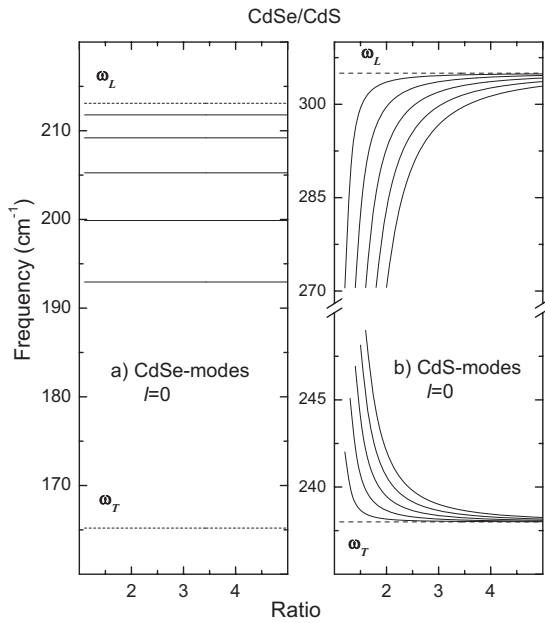


FIG. 1. Optical-phonon modes at $P=0$ for $l=0$ in CdSe/CdS core-shell hybrid quantum dots as a function of the ratio b/a . Panel (a) CdSe core modes and panel (b) CdS shell modes. In the calculation we fixed the value of $a=30$ Å. The bulk LO- and TO-phonon frequencies are indicated by dashed lines.

strongly on the ratio $\gamma=b/a$ converging either to the bulk values ω_L or to ω_T as $\gamma \rightarrow \infty$.

In Fig. 1(a), the first five LO modes of the CdSe core are shown in the upper half of the figure, whereas the transversal CdSe core modes all are concentrated in a single line, in close coincidence with the ω_T value for bulk CdSe. This latter result is due to the very low value of β_T for this case, in contrast to the large value of β_L needed to describe the

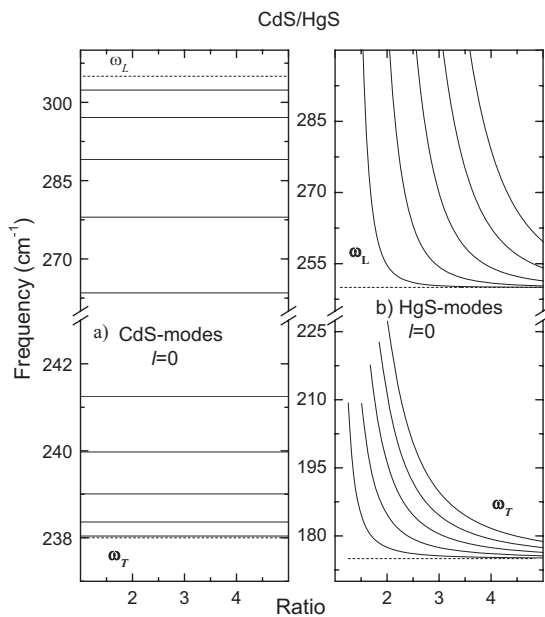


FIG. 2. The same as in Fig. 1 for CdS/HgS core-shell hybrid quantum dot. Panel (a) CdS core modes and panel (b) HgS shell modes.

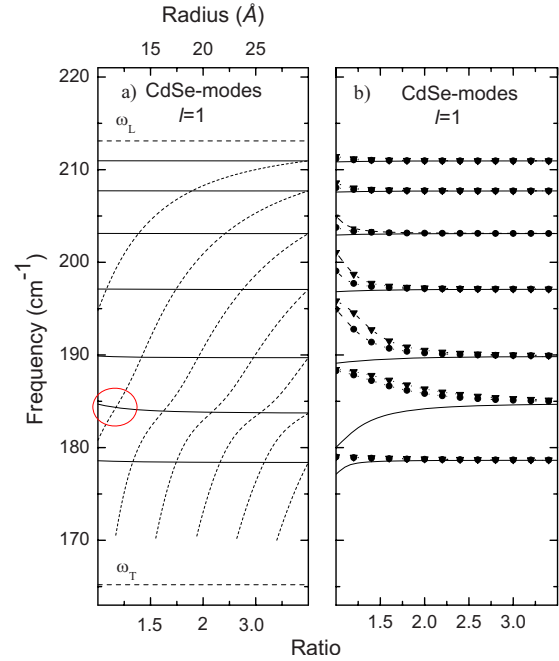


FIG. 3. (Color online) Optical core-phonon modes for $l=1$ in various CdSe/CdS quantum dot systems. Panel (a), solid line show CdSe core modes in CdSe/CdS hybrid particles versus b/a (bottom scale) for $a=30$ Å. Dashed lines show $l=1$ modes of bare CdSe spherical dots in a uniform dielectric medium versus the dot radius R (top scale). In these calculations $\epsilon_D=4.64$. Panel (b), similar to the solid lines in panel (a) but for $\epsilon_{2\infty}/\epsilon_D=0.5$ (line), 3 (line triangles), and 6 line diamonds.

downward curvature of the bulk CdSe longitudinal phonon branch. Figure 1(b) presents the frequency dependence of the slab CdS modes as a function of the ratio b/a . For the longitudinal modes the frequency presents a growing character as the ratio $\gamma=b/a$ increases while for the transversal modes the opposite dependence is seen. The chosen interval for γ is actually very large and, as can be observed, the frequencies display a rapid trend toward their bulk values.

Figure 2 shows the same kind of plot for the CdS/HgS core-shell nanostructure. The structure of the figure is the same as in Fig. 1 and we shall focus on the main material-related differences. In the CdS core region [Fig. 2(a)], both the longitudinal (upper section) and transversal (lower section) mode frequencies are shown but now five separated values of the frequency are clearly seen for the transversal modes (the β_T parameter for CdS is not so small). The longitudinal frequencies are again all lower than the bulk value but the transversal frequencies are higher than ω_T . The main differences are seen in the HgS shell modes [Fig. 2(b)]. The frequencies for the longitudinal modes (upper section) present a decreasing character for growing values of b/a and a rapid trend toward the HgS bulk frequency ω_L . The frequencies for the transversal modes (lower section) are also decreasing functions of the ratio b/a . In both cases we observe that very large frequencies are obtained when $\gamma \rightarrow 1$. It is worth remarking that the oscillation frequencies have a natural upper bound for obvious physical reasons; they cannot be higher than the corresponding bulk semiconductor

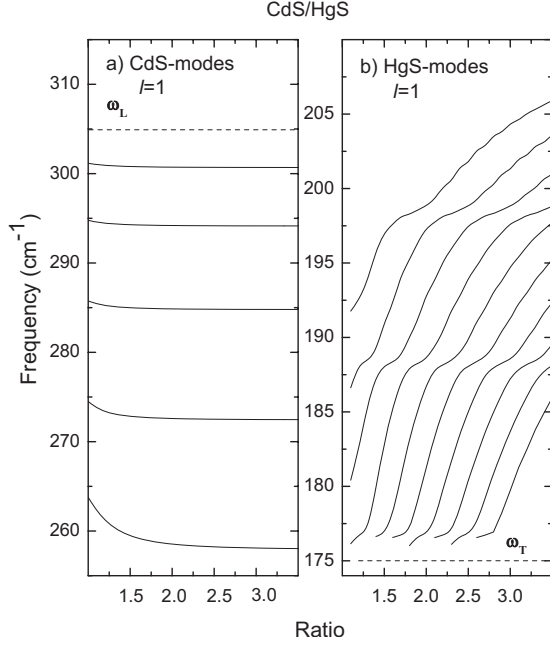


FIG. 4. The same as in Fig. 2 for the $l=1$ phonon modes of CdS/HgS nanoparticles. Panel (a) CdS core modes and panel (b) HgS shell modes. In the calculation $\epsilon_D=4.64$ and $a=30$ Å.

value of the frequency at the Brillouin-zone boundary (for $\kappa \sim \pi/a_0$ with a_0 the lattice constant).

The case of $l=1$ for the CdSe/CdS core modes is displayed in Fig. 3. Here, the dispersion curves are calculated from the solutions of Eq. (A5) and describe coupled phonon modes of mixed nature. In Fig. 3(a), the solid lines are computed as a function of b/a for CdSe/CdS particles with constant $a=30$ Å while the dashed lines correspond to a strictly spherical CdSe quantum dot embedded in a host material

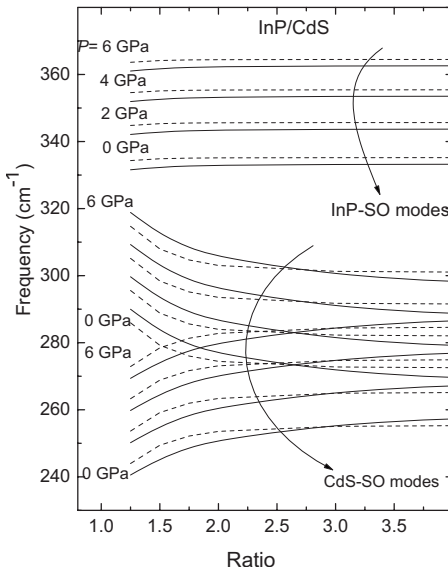


FIG. 5. Calculated interface optical-phonon frequencies for an InP/CdS core-shell nanostructure as a function of b/a for $l=1$ (solid line) and $l=2$ (dashed lines). The curves correspond to the InP- and two CdS-SO phonon branches given by Eq. (31) for different values of the hydrostatic pressure $P=0, 2, 4,$ and 6 GPa.

TABLE III. Values of parameters used for the calculation of the phonon modes of InP/CdS hybrid nanoparticles under pressure as plotted in Fig. 5 and in the fitting of Fig. 7 (Ref. 27). The temperature coefficients are used to shift the $P=0$ values of ω_L and ω_T consistent with the observed 80 K laser heating of the samples.

Parameters	InP ^a	CdS ^b
ω_L (cm ⁻¹)	344.5	301.7
$\frac{d\omega_L}{dP}$ (cm ⁻¹ GPa ⁻¹)	5.4	4.8
ω_T (cm ⁻¹)	303.3	231.7
$\frac{d\omega_T}{dP}$ (cm ⁻¹ GPa ⁻¹)	5.8	4.8
$\frac{d\omega_L}{dT}$ (cm ⁻¹ K ⁻¹)	-0.015	-0.026 ^c
$\frac{d\omega_T}{dT}$ (cm ⁻¹ K ⁻¹)	-0.018	-0.024 ^c
ϵ_∞	9.6 ^c	5.4 ^b
$\frac{d\epsilon_\infty}{dP}$ (GPa ⁻¹)	-0.106 ^d	-0.054

^aReference 48.

^bReference 42.

^cReference 43.

^dCalculated, see Wang *et al.*, Ref. 48.

with $\epsilon_D=4.6$. In general, for a fixed core radius we observe the same weak dependence on the ratio b/a as in Figs. 1 and 2. However, now one can see some bending in the dispersion caused by the interaction with the electrostatic potential of the surface oscillation. This character in the core-mode dispersion of the CdSe/CdS hybrid particle is indicated by a circle where the interaction of the LO-confined phonon with the surface mode becomes strong for a certain value of the ratio b/a . Figure 3(b) shows the dependence on γ of the first seven eigenfrequencies for the CdSe-core phonons in the hybrid nanoparticle when changing the dielectric constant ϵ_D of the host material. We have fixed the values of $\epsilon_{i\infty}$ ($i=1, 2$) at $P=0$ according to Table I, and have taken $\epsilon_{2\infty}/\epsilon_D=0.5, 3,$ and 6 . We observe strong dependence on the dielectric constant ϵ_D and, also, that the sign (\pm) of the curvature of ω versus γ depends on the value of $\epsilon_{2\infty}/\epsilon_D$, being (+) for $\epsilon_{2\infty}/\epsilon_D > 1$ and (-) for $\epsilon_{2\infty}/\epsilon_D < 1$. Finally, notice that the phonon frequencies approach asymptotically to the same value independent of ϵ_D as b/a increases. For larger values of b/a , the influence of the outer medium becomes negligible and we can consider the CdSe quantum dot as embedded in a host CdS material.

Figure 4 is devoted to the $l=1$ core and shell modes found for the CdS/HgS hybrid nanostructure system. In the panel (a) we observe the same trends as in the case of Fig. 3(a) for the core modes (again $a=30$ Å), where difference arises only through the value of the physical parameters used in each of the core-shell nanostructures, and through the stronger interaction with the electrostatic potential surface modes close to $\gamma=1$. Panel (b) shows the Hg-shell modes near the bulk transversal HgS phonon frequency ω_T , as calculated using Eq. (B7). In this case, the HgS bulk phonon dispersion increases as the phonon wave vector increases (see Table II) and hence we have a set of confined phonons above ω_T well separated in frequency for $a=30$ Å. The frequencies present an increasing character for growing values of b/a while they rapidly trend toward the HgS bulk frequency ω_T for $b \rightarrow a$.

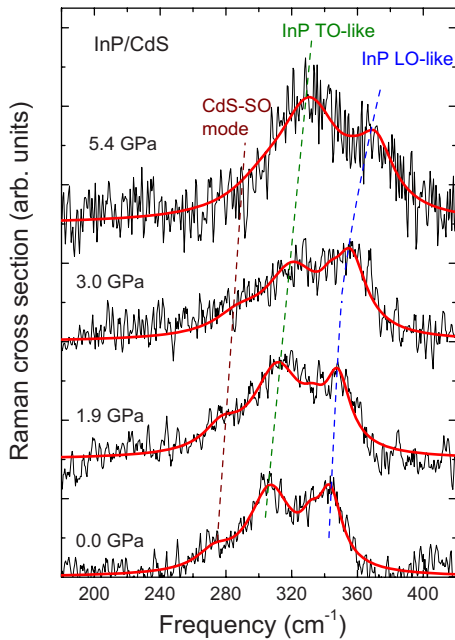


FIG. 6. (Color online) Raman spectra at 373 K for InP/CdS nanoparticles at different pressures (adapted from Ref. 27). The pressure media are pyridine for the 0.0 GPa trace and 4:1 methanol:ethanol for the other traces (Ref. 58). Dashed lines indicate dependence of the InP confined LO and TO phonons, and the CdS SO mode on the pressure. Solid curves are PMA-based line-shape simulations using the best-fit results of Fig. 7.

This result contrasts with the case of $l=0$ where we are dealing with purely confined phonons. Also from Fig. 4(b), we observe three surface modes whose interaction with the confined shell modes causes the bending in the dispersion curves near 176, 188, and 198 cm^{-1} , and we learn that for large values of γ the core-shell SO phonon frequencies are roughly independent of the γ . The strong mixture between LO and TO, and the interaction with the electrostatic potential are directly responsible for the dispersion of the shell modes seen in Fig. 4(b) as a function of the ratio b/a .

Infrared and Raman spectroscopies are frequently used to investigate the surface-optical phonons in nanoparticles.^{26,33,49–54} Figure 5 shows the effect of hydrostatic pressure on the dispersion relations of the surface-optical-phonon frequencies in InP/CdS core-shell nanoparticles. In the present calculation we used the semiconductor parameters given in Table III. To account for the pressure dependence of the medium's dielectric function we employed $\epsilon_D(P) = 13.9 + 0.013P$ with P in GPa, corresponding to the observed $\epsilon_D(P)$ of pyridine, a pressure medium used in our diamond-anvil cell (DAC) experiments.^{27,55} Table III values are chosen within the range of accepted experimental results for bulk InP and CdS (for $d\epsilon_\infty/dP$ in InP the theoretical value of Wang *et al.*⁴⁸ is used), and again we neglect the effects of internal strain at the InP-CdS interface. We can expect this to be quite small compared to the variations in the literature values, which typically are a few inverse cm for ω_L and ω_T , and $\sim 5\text{--}15\%$ for the pressure and temperature coefficients.⁵⁶ In Fig. 5 we display three types of surface vibration modes obtained from Eq. (31) for values of the

hydrostatic pressure $P=0, 2, 4,$ and 6 GPa, and $l=1$ and 2 . The upper branches represent the SO frequencies of the InP core, which practically do not change with the values of γ . However we see that $\omega(b/a, P)$ increases as the pressure is raised. These frequencies can be considered to be the SO phonon modes of an InP spherical quantum dot imbedded in an “effective dielectric medium $\epsilon_{D, \text{eff}}(P)$.”⁴⁰ The two lower sets of branches give the frequencies of the shell CdS-SO phonons, and they correspond to the interface optical modes of a spherical quantum well sandwiched between a spherical InP dot and an infinite host dielectric medium. In contrast to the interface modes of the InP core, the upper (lower) SO modes of the CdS shell decrease (increase) strongly as γ increases, but the three sets of modes present the same increasing trend with pressure.

The interface optical phonons are directly dependent on the core/shell geometry via Eq. (31) and strongly so for the shell's SO modes in InP/CdS nanoparticles (see Fig. 5). Hence, the first-order Raman technique provides potentially sensitive means to determine of the growth parameter $\gamma = b/a$, in addition to yielding information on the core radius through the a dependence inherent in the confined core modes [Eqs. (22) and (23)] that are observed using the Raman effect.

We point out that the intensities of interface phonon contributions to the first-order-assisted scattering of light are linked to the breakdown of the Raman selection rules in spherical QDs and can be further affected if some nonspherical symmetry is present in the quantum dots.⁴⁰ For as-grown ensembles of nominally spherical quantum dots, the frequencies of the observed peaks and shoulders are closely related to the different types of core and/or shell modes described in Secs. III and IV.

V. HIGH-PRESSURE RAMAN RESULTS IN CORE-SHELL NANOPARTICLES

A Raman-scattering study was performed on the effects of applied hydrostatic pressure on InP/CdS hybrid nanoparticles. The samples are fabricated by a two-stage colloidal chemistry process,^{14,27} and presented an ensemble of nearly spherical nanoparticles with InP cores ranging in diameters from 40–60 Å, coated by CdS shells having outer diameters in the range 50–90 Å, as indicated by photoluminescence, x-ray, and electron microscopy characterization.^{27,57} High-pressure Raman spectra were measured at room temperature using DAC. The Stokes-to-anti-Stokes ratio showed ~ 80 K laser (at 5 mW power) heating of the samples. Raman spectra recorded at different pressures are displayed in Fig. 6. Two peaks can be seen due to the InP confined LO- and TO-phonon modes, and a broad low-frequency shoulder contributing to the tail of the TO peak is detected. The latter feature is assigned to the SO phonons of the CdS shell. The solid curves are line-shape simulations of the Raman spectra based on the PMA calculations, as discussed below.

The Raman cross section shown in Fig. 6 presents an anomaly which is not common in II-VI nanocrystal, i.e., the appearance of the TO phonon line with an almost equal intensity to the LO peak at any applied pressure. It is well

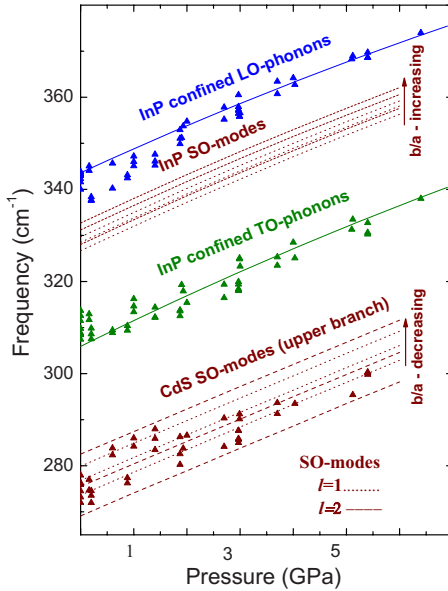


FIG. 7. (Color online) Calculation of the pressure dependence of the phonon frequencies for the InP-confined LO and TO phonons (solid lines), and for the InP SO modes at the core-shell interface as well as for the upper branch CdS SO modes at the shell outer surface (dotted lines for $l=1$ and dashed lines for $l=2$). SO frequencies are computed for $b/a=1.2, 1.3,$ and 1.4 (or $1.1, 1.2,$ and 1.3) in the case of $l=1$ (or $l=2$). Triangles are experimental data from Fig. 6 and also Ref. 27.

documented that in the first-order resonant Raman scattering of II-VI colloidal nanocrystals the TO vibration peak is absent. In spherical quantum dots the translational symmetry is broken. Then the stronger Fröhlich interaction (F) associated only with the LO oscillation becomes dipole allowed and dominates over the weaker deformation-potential (DP) dipole coupling allowed for both TO and LO. Hence, typical spectra show a peak centered at the confined LO mode frequency with an asymmetric low-energy wing. The presence of the blueshifted TO vibration in InP/CdS and other InP-based nanoparticles indicates an anomalously large contribution of the DP interaction. The strong TO signal cannot be explained in terms of the nonconservation of the translational symmetry but by the dependence of the intensity on the quantum-dot radius (R) and the interplay between the DP and F exciton-phonon coupling constants. In Ref. 52 it is shown that the Raman intensity is proportional to $1/R$ for the F mechanism; while in the case of the DP mechanism the dependence is $1/R^3$. Thus, for decreasing radius, the contribution of the DP relative to the F cross section enhances as $1/R^2$. Also, compared to typical II-VI materials, the lower ionic charge (lower Fröhlich coupling constant) and the larger value of the optical deformation-potential characteristic of InP, explain the observed important role of the DP mechanism.

For this sample studied in Fig. 6, with 45 \AA mean core diameter, the observed 1.7 cm^{-1} and 1.4 cm^{-1} shifts at $P=0$ in the confined LO- and TO-phonon frequencies from the bulk values are related, respectively, to the decreasing and increasing dependence of the InP bulk frequencies on the phonon wave vector (see Tables II and III). The observed

line broadening of the LO- and TO-phonon peaks is mainly due to the distribution of core diameters in the sample ensemble. Likewise, based on the theoretical predictions for the dependence of the interface modes on b/a [Eq. (31)], the size distribution in the ensemble should also contribute appreciably to the width of the shoulder arising from the SO modes of the CdS shell. In Fig. 6 we observe that the LO and TO peak positions are shifted to higher energy with increasing pressure. Also, the low-frequency SO shoulder appears to follow the same pressure dependence trend as P increases. A guide to the pressure-induced shifts of the assigned phonon modes is indicated by the dashed lines in this figure.

In Fig. 7 the solid triangles show the positions of the measured LO, TO, and SO features as a function of P . The frequencies $\omega(P)$ were obtained by successive three-peak empirical fits to the spectra using the iterative method described in Ref. 27 to reduce the random scatter in the pressure dependence of the data points. The curves in Fig. 7 give the theoretical mode frequencies calculated as a function of pressure following the PMA model described above with the core radius varied to optimize the agreement with the data for the confined LO- and TO-core phonons. The latter confined-mode results, calculated according to Eqs. (22) and (23), are shown by the solid curves, while several solutions of Eq. (31) for the InP-core SO modes and the CdS SO modes are represented by the dots ($l=1, b/a=1.2, 1.3,$ and 1.4) and dashed curves ($l=2, b/a=1.1, 1.2,$ and 1.3). In the calculation we have used the values $\beta_L=17.4 \times 10^3 \text{ cm}^{-1} \text{ \AA}$ and $\beta_T=7.0 \times 10^3 \text{ cm}^{-1} \text{ \AA}$ for InP.⁵² From the best fit for the pressure dependence of the mode frequencies obtained in the PMA calculations to both the confined-mode and the SO-mode data, we have extracted the values of $2a=45 \pm 10 \text{ \AA}$ and $b/a=1.2$. Overall, the agreement with the Raman results in Fig. 7 shows that the theory can reproduce quite nicely the observed pressure dependence of the LO-, TO-, and SO-phonon modes in InP/CdS hybrid nanoparticles. To further test the agreement between theory and experiment, the final results of the PMA calculations are used to simulate the spectral line shapes in Fig. 6 (bold solid curves). Four Lorentzian peaks are included in this case to account for the LO- and TO-confined modes and the outer-surface CdS SO modes observed in the spectra, as well as the InP SO modes expected to contribute to the unresolved background between the LO and TO peaks. For simplicity $l=2$ and $b/a=1.2$ are used to compute the SO modes. Adjusting the heights and widths of the four peaks then optimizes the simulations. As seen in Fig. 6, the results give a satisfactory representation of the spectra.

VI. CONCLUSIONS

In summary, we have implemented a direct calculation of the coupled optical-phonon modes in spherical core-shell hybrid nanostructures under applied high hydrostatic pressure. The extended phenomenological macroscopic approach used to study the optical phonons in core/shell nanoparticle systems allows the description of the main characteristics of the oscillations in these structures at all pressures within the regime of linear elastic response. We showed that the shell

phonon modes are very sensitive to the spatial geometrical ratio b/a while the core modes are almost independent of the capping shell thickness. For the corelike and shell-like surface phonons, which involve a long-range electric potential, we found that their frequencies increase with P , and calculated the pressure-induced shifts for a given value of the ratio b/a . The effects of the pressure on the optical oscillations show the same trends as for the bulk optical phonons. The present PMA calculations are confirmed by direct measurements of the pressure dependence of the first-order Raman scattering in InP/CdS hybrid nanoparticles.

Investigations of the effects of high pressure on the Raman spectra of optical-phonon frequencies in core/shell semiconductor nanoparticles can enhance our understanding of several important properties in these complex systems. In addition to providing direct knowledge about the vibrational properties of the hybrid nanoparticles under pressure, such studies, informed by the PMA theory developed here, can yield useful information on the β_T and β_L parameters gov-

erning the bulk phonon dispersion at the Γ point of the Brillouin zone, and also on the geometric dimensions a and b which are significant factors for controlling the growth and applications of semiconductor hybrid nanoparticles.

ACKNOWLEDGMENTS

This work was partially supported by Brazilian agencies FAPESP and CNPq. G.E.M. and C.T.-G. are grateful for the Visiting Scholar Program of the ICTP/Trieste. We gratefully acknowledge the assistance of Y. Sahoo, D. W. Lucey, and P. N. Prasad for growth of the nanoparticle samples, and F. Manciu for sample characterization studies.

APPENDIX A: PHONON DISPERSION IN THE CORE

In this case the boundary conditions at $r=a(P)$ and $r=b(P)$ lead to the equations

$$\begin{pmatrix} l\bar{\epsilon}_{1\infty} + l + 1 & -\bar{\epsilon}_{1\infty}v_1j_l'(v_1) - (l+1)j_l(v_1) & -(2l+1) & 0 \\ (\bar{\epsilon}_{2\infty} - 1) & -(\bar{\epsilon}_{2\infty} - 1)j_l(v_1) & -\bar{\epsilon}_{2\infty}\left(\frac{l\gamma^{2l+1}}{l+1} + 1\right) - \gamma^{2l+1} + 1 & 0 \\ lK_1 & \mu_1^2v_1j_l'(v_1) & 0 & -l(l+1)v_1^2j_l(\mu_1) \\ \sqrt{l(l+1)}K_1 & \sqrt{l(l+1)}\mu_1^2j_l(v_1) & 0 & -\sqrt{l(l+1)}f_l(\mu_1)v_1^2 \end{pmatrix} \begin{pmatrix} A^{(1)} \\ A^{(2)} \\ A^{(3)} \\ A^{(4)} \end{pmatrix} = 0 \quad (\text{A1})$$

with $K_1 = [\omega_{1L}^2(P) - \omega_{1T}^2(P)]a^2(P)/\beta_{1T}^2$, $f_l(\mu_1) = j_l(\mu_1) + \mu_1j_l'(\mu_1)$, $\bar{\epsilon}_{1\infty} = \epsilon_{1\infty}(P)/\epsilon_{2\infty}(P)$, $\bar{\epsilon}_{2\infty} = \epsilon_{2\infty}(P)/\epsilon_D(P)$, and $A^{(2(4)}/A^{2(4)} = [4\pi\alpha_1(P)a^2(P)]/[\epsilon_{1\infty}(P)v_1^2]$.

The above system of linear homogeneous equations determines the constants (up to a normalization constant) and the dispersion law for the coupled modes in the core. Considering the general case when $l \geq 0$, we must require the determinant of this system to be equal to zero, providing us with the Eq. (20) where

$$F_l(\mu; P) = [l\bar{\epsilon}_{1\infty} + l + 1]\mu^2f_l(\mu_1) - \bar{\epsilon}_{1\infty}K_1lp_l(\mu) - (\bar{\epsilon}_{2\infty} - 1) \times (2l+1)(l+1)\frac{\mu^2}{\Omega_l(\gamma)}f_l(\mu), \quad (\text{A2})$$

$$G_l(\mu; P) = [l\bar{\epsilon}_{1\infty} + l + 1]\mu^2j_l(\mu) + K_1p_l(\mu) - (\bar{\epsilon}_{2\infty} - 1)\frac{(2l+1)}{\Omega_l}[(l+1)\mu^2j_l(\mu) + K_1p_l(\mu)], \quad (\text{A3})$$

$$\Omega_l = (l+1)(\bar{\epsilon}_{2\infty} - 1) + (l\bar{\epsilon}_{2\infty} + l + 1)\gamma^{2l+1}(P), \quad (\text{A4})$$

and $p_l(\mu) = lj_l(\mu) - \mu j_l'(\mu)$. In the case of $l=1$ we can derive from Eq. (A1) and for $Q_1^2 < 0$ and $q_1^2 > 0$, that the coupled solutions satisfy

$$2\frac{[1 - v_1 \cot(v_1)]}{2v_1 \cot(v_1) + (v_1^2 - 2)} = \frac{E(P)\mu^2[(\mu^2 + 1) - \mu \coth(\mu)] + K_1\bar{\epsilon}_{1\infty}[3\mu \coth(\mu) - (3 + \mu^2)]}{E(P)\mu^2[\mu \coth(\mu) - 1] - K_1\left[1 - 3\frac{(\bar{\epsilon}_{2\infty} - 1)}{\Omega_1}\right][3\mu \coth(\mu) - (3 + \mu^2)]} \quad (\text{A5})$$

with

$$E(P) = \overline{\epsilon_{1\infty}} + 2 - 6 \frac{(\overline{\epsilon_{2\infty}} - 1)}{\Omega_1}.$$

APPENDIX B: PHONON DISPERSION IN THE SHELL

Additional boundary conditions of the type given in Eq. (4) for the electric potential φ , as well as the mechanical

vector displacement condition $\mathbf{u}|_S=0$, when applied at the spherical surfaces $r=a(P)$ and $r=b(P)$ provide us with the equations

$$l\nu_2^2(\overline{\epsilon_{1\infty}} - 1)B^{(1)} + \nu_2^2(l\overline{\epsilon_{1\infty}} + l + 1)B^{(2)} - [l\overline{\epsilon_{1\infty}}j_l(\nu_2) - \nu_2j_l'(\nu_2)]B^{(3)} + [l\overline{\epsilon_{1\infty}}n_l(\nu_2) - \nu_2n_l'(\nu_2)]B^{(4)} = 0, \quad (\text{B1})$$

$$\nu_2^2[(l+1) + l\overline{\epsilon_{2\infty}}]B^{(1)} + \frac{(l+1)\nu_2^2}{\gamma^{2l+1}(P)}(1 - \overline{\epsilon_{2\infty}})B^{(2)} - \frac{1}{\gamma'(P)}\{(l+1)j_l[\gamma(P)\nu_2] + \gamma(P)\nu_2\overline{\epsilon_{2\infty}}j_l'[\gamma(P)\nu_2]\}B^{(3)} - \frac{1}{\gamma'(P)}\{(l+1)n_l[\gamma(P)\nu_2] + \gamma(P)\nu_2\overline{\epsilon_{2\infty}}n_l'[\gamma(P)\nu_2]\}B^{(4)} = 0, \quad (\text{B2})$$

$$K_2\nu_2[lB^{(1)} - (l+1)B^{(2)}] + \mu_2^2[B^{(3)}j_l'(\nu_2) + B^{(4)}n_l'(\nu_2)] - l(l+1)\nu_2[B^{(5)}j_l(\mu_2) + B^{(6)}n_l(\mu_2)] = 0, \quad (\text{B3})$$

$$\sqrt{l(l+1)}\{\nu_2^2K_2[B^{(1)} + B^{(2)}] + \mu_2^2[B^{(3)}j_l(\nu_2) + B^{(4)}n_l(\nu_2)] - \nu_2^2[B^{(5)}f_l(\mu_2) + B^{(6)}\tilde{f}_l(\mu_2)]\} = 0, \quad (\text{B4})$$

$$\gamma'(P)\nu_2K_2\left[lB^{(1)} - \frac{l+1}{\gamma^{2l+1}(P)}B^{(2)}\right] + \gamma(P)\mu_2^2[B^{(3)}j_l'(\gamma(P)\nu_2) + B^{(4)}n_l'(\gamma(P)\nu_2)] - l(l+1)\nu_2[B^{(5)}j_l(\gamma(P)\mu_2) + B^{(6)}n_l(\gamma(P)\mu_2)] = 0, \quad (\text{B5})$$

$$\sqrt{l(l+1)}\left\{\gamma'(P)\nu_2^2K_2\left[B^{(1)} + \frac{1}{\gamma^{2l+1}(P)}B^{(2)}\right] + \mu_2^2\{B^{(3)}j_l[\gamma(P)\nu_2] + B^{(4)}n_l[\gamma(P)\nu_2]\} - \nu_2^2\{B^{(5)}f_l[\gamma(P)\mu_2] + B^{(6)}\tilde{f}_l[\gamma(P)\mu_2]\}\right\} = 0, \quad (\text{B6})$$

where $\tilde{f}_l(z)$ is analogous to the former $f_l(z)$ but now $j_l(z)$ is replaced by $n_l(z)$. In the latter equations $K_2 = [\omega_{2L}^2(P) - \omega_{2T}^2(P)]a^2(P)/\beta_{2T}^2$ and $B^{(i)} = 4\pi\alpha_2(P)a^2(P)/[\epsilon_{2\infty}(P)]B^{(i)}$ for $i=3,4,5,6$.

Equations (B1)–(B6) are a 6×6 system of linear homogeneous equations defining the constants $B^{(i)}$ (up to the normalization constant). Requiring the system's determinant to be zero, we are led to the dispersion law for the coupled oscillations. The latter determinant equation gives us the shell phonon frequencies for the different coupled modes as a function of the geometric parameter $\gamma(P)$. The determinant describing the phonon modes for a spherical slab is given by

$$\begin{vmatrix} l & -1 & j_l'(\nu_2) & n_l'(\nu_2) & -lj_l(\mu_2) & -ln_l(\mu_2) \\ \nu_2 & \frac{\nu_2}{l+1} & j_l(\nu_2) & n_l(\nu_2) & \frac{-\nu_2f_l(\mu_2)}{l+1} & \frac{-\nu_2\tilde{f}_l(\mu_2)}{l+1} \\ l\gamma(P) & \frac{-1}{\gamma^{l+1}(P)} & \gamma(P)j_l'[\gamma(P)\nu_2] & \gamma(P)n_l'[\gamma(P)\nu_2] & -lj_l[\gamma(P)\mu_2] & -ln_l[\gamma(P)\mu_2] \\ \gamma(P)\nu_2 & \frac{\nu_2}{(l+1)\gamma^{l+1}(P)} & j_l[\gamma(P)\nu_2] & n_l[\gamma(P)\nu_2] & \frac{-\nu_2f_l[\gamma(P)\mu_2]}{l+1} & \frac{-\nu_2\tilde{f}_l[\gamma(P)\mu_2]}{l+1} \\ l\nu_2(\overline{\epsilon_{1\infty}} - 1) & \frac{\nu_2l}{l+1}\overline{\epsilon_{1\infty}} + \nu_2 & -h_l(\nu_2) & -\tilde{h}_l(\nu_2) & 0 & 0 \\ \nu_2(l+1 + l\overline{\epsilon_{2\infty}}) & \frac{\nu_2}{\gamma^{2l+1}(P)}(1 - \overline{\epsilon_{2\infty}}) & g_l[\gamma(P)\nu_2] & \tilde{g}_l[\gamma(P)\nu_2] & 0 & 0 \end{vmatrix} = 0. \quad (\text{B7})$$

We have now introduced the notation

$$h_l(x) = K_2(P)[l\overline{\epsilon_{1\infty}}j_l(x) - xj_l'(x)]/\mu_2^2,$$

$$\tilde{h}_l(x) = K_2(P)[l\overline{\epsilon_{1\infty}}n_l(x) - xn_l'(x)]/\mu_2^2,$$

$$g_l(x) = -K_2(P)[(l+1)j_l(x) + \overline{\epsilon_{2\infty}}xj_l'(x)]/[\mu_2^2\gamma'(P)],$$

$$\tilde{g}_l(x) = -K_2(P)[(l+1)n_l(x) + \overline{\epsilon_{2\infty}}xn_l'(x)]/[\mu_2^2\gamma'(P)].$$

- ¹X. Peng, L. Manna, W. Yang, J. Wickham, E. Scher, A. Kadanavich, and A. P. Alivisatos, *Nature (London)* **404**, 59 (2000).
- ²L.-S. Li, J. Hu, W. Yang, and A. P. Alivisatos, *Nano Lett.* **1**, 349 (2001).
- ³V. P. Puntès, K. M. Krishnan, A. P. Alivisatos, *Science* **291**, 2115 (2001).
- ⁴G. Cantele, D. Ninno, and G. Iadonisi, *Phys. Rev. B* **64**, 125325 (2001).
- ⁵G. Cantele, G. Piacente, D. Ninno, and G. Iadonisi, *Phys. Rev. B* **66**, 113308 (2002).
- ⁶D. Katz, T. Wizansky, O. Millo, E. Rothenberg, T. Mokari, and U. Banin, *Phys. Rev. Lett.* **89**, 086801 (2002).
- ⁷X. Chen, A. Nazzal, D. Goorskey, M. Xiao, Z. A. Peng, and X. Peng, *Phys. Rev. B* **64**, 245304 (2001).
- ⁸A. Mews, A. Eychmüller, M. Giersig, D. Schooss, and J. Weller, *J. Phys. Chem.* **98**, 934 (1994).
- ⁹D. Schooss, A. Mews, A. Eychmüller, and H. Weller, *Phys. Rev. B* **49**, 17072 (1994).
- ¹⁰A. Mews, A. V. Kadavanich, U. Banin, and A. P. Alivisatos, *Phys. Rev. B* **53**, R13242 (1996).
- ¹¹F. Koberling, A. Mews, and T. Basché, *Phys. Rev. B* **60**, 1921 (1999).
- ¹²H. E. Porteanu, E. Lifshitz, M. Pflughoefft, A. Eychmüller, and H. Weller, *Phys. Status Solidi B* **226**, 219 (2001).
- ¹³M. Shim, C. Wang, and P. Guyot-Sionnest, *J. Phys. Chem. B* **105**, 2369 (2001).
- ¹⁴D. Lucey, D. MacRae, M. Furis, Y. Sahoo, A. Cartwright, and P. Prasad, *Chem. Mater.* **17**, 3754 (2005).
- ¹⁵R. Ruppini and R. Englman, *Rep. Prog. Phys.* **33**, 149 (1970).
- ¹⁶M. C. Klein, F. Hache, D. Ricard, and C. Flytzanis, *Phys. Rev. B* **42**, 11123 (1990).
- ¹⁷S. Nomura and T. Kobayashi, *Phys. Rev. B* **45**, 1305 (1992).
- ¹⁸D. V. Melnikov and W. B. Fowler, *Phys. Rev. B* **64**, 245320 (2001).
- ¹⁹M. T. Kach, V. Holovatsky, O. Voitsekhivska, M. Mykhalyova, and R. Fartushynsky, *Phys. Status Solidi B* **225**, 331 (2001).
- ²⁰F. Comas, C. Trallero-Giner, N. Studart, and G. E. Marques, *Phys. Rev. B* **65**, 073303 (2002).
- ²¹F. Comas, C. Trallero-Giner, N. Studart, and G. E. Marques, *J. Phys.: Condens. Matter* **14**, 6469 (2002).
- ²²E. Roca, C. Trallero-Giner, and M. Cardona, *Phys. Rev. B* **49**, 13704 (1994).
- ²³F. Comas and C. Trallero-Giner, *Physica B* **192**, 394 (1993).
- ²⁴C. Trallero-Giner and F. Comas, *Philos. Mag. B* **70**, 583 (1994).
- ²⁵C. Trallero-Giner, R. Pérez, and F. García-Moliner, *Long Wave Polar Optical Modes in Semiconductor Heterostructures* (Pergamon Press, New York, 1998).
- ²⁶A. V. Baranov, Yu. P. Rakovich, J. F. Donegan, T. S. Perova, R. A. Moore, D. V. Talapin, A. L. Rogach, Y. Masumoto, and I. Nabiev, *Phys. Rev. B* **68**, 165306 (2003).
- ²⁷R. E. Tallman, B. A. Weinstein, C. Trallero-Giner, Y. Sahoo, and P. N. Prasad, *Phys. Status Solidi B* **246**, 477 (2009).
- ²⁸M. Haase and A. Alivisatos, *J. Phys. Chem.* **96**, 6756 (1992).
- ²⁹J. Schroeder and P. Persans, *J. Lumin.* **70**, 69 (1996).
- ³⁰V. Swamy, A. Kuznetsov, L. S. Dubrovinsky, P. F. McMillan, V. B. Prakapenka, G. Shen, and B. C. Muddle, *Phys. Rev. Lett.* **96**, 135702 (2006).
- ³¹H. M. Fan, Z. H. Ni, Y. P. Feng, X. F. Fan, J. L. Kuo, Z. X. Shen, and B. S. Zou, *Appl. Phys. Lett.* **90**, 021921 (2007).
- ³²J. S. Reparaz, A. Bernardi, A. R. Goni, M. I. Alonso, and M. Garriga, *Phys. Status Solidi B* **246**, 482 (2009); J. S. Reparaz, A. Bernardi, A. R. Goni, P. Lacharmoise, M. I. Alonso, M. Garriga, J. Novak, and I. Vavra, *Appl. Phys. Lett.* **91**, 081914 (2007).
- ³³B. Weinstein, *Phys. Status Solidi B* **244**, 368 (2007).
- ³⁴The Gruneisen parameters vary by $\sim 20\%$ across the Brillouin zone in bulk semiconductors, see B. A. Weinstein and R. Zallen, in *Light Scattering in Solids*, edited by M. Cardona and G. Guntherodt (Springer, Berlin, 1984), Vol. IV, p. 463. The present approximation of P -independent β_L and β_T is not strictly valid and it becomes worse for smaller nanoparticles. In particles of the size studied here the neglected variation is a small higher order effect.
- ³⁵In Ref. 39, Sec. 3, it was shown quantitatively that for a frequency difference between the bulk optical-phonon branches at the zone center of $\Delta\omega \sim 6 \text{ cm}^{-1}$ the matching condition of the normal component of the force flux can be replaced by $\mathbf{u}=0$ at the surface. According to the values given in Tables I and III for the LO and TO bulk phonon frequencies of the core/shell hybrid heterostructures studied in this work, we obtain $\Delta\omega > 40 \text{ cm}^{-1}$, which justifies using the infinite barrier model for the optical oscillation.
- ³⁶P. M. Morse and H. Feshbach, *Methods of Theoretical Physics* (McGraw-Hill, New York, 1953).
- ³⁷M. Abramowitz and I. Stegun, *Handbook of Mathematical Functions* (Dover, NY, 1972).
- ³⁸F. Comas, C. Trallero-Giner, S. J. Prado, G. E. Marques, and E. Roca, *Phys. Status Solidi B* **243**, 459 (2006).
- ³⁹R. Pérez-Alvarez, F. García-Moliner, V. Velasco, and C. Trallero-Giner, *J. Phys.: Condens. Matter* **5**, 5389 (1993).
- ⁴⁰F. Comas and C. Trallero-Giner, *Phys. Rev. B* **67**, 115301 (2003).
- ⁴¹C. Trallero-Giner, A. Debernardi, M. Cardona, E. Menéndez-Proupín, and A. I. Ekimov, *Phys. Rev. B* **57**, 4664 (1998).
- ⁴²M. P. Chamberlain, C. Trallero-Giner, and M. Cardona, *Phys. Rev. B* **51**, 1680 (1995); U. Venkateswaran, M. Chandrasekhar, and H. R. Chandrasekhar, *ibid.* **30**, 3316 (1984); G. A. Samara, *ibid.* **27**, 3494 (1983).
- ⁴³*Semiconductors: Intrinsic Properties of Group IV Elements and III-V, II-VI and I-VII Compounds, Semimagnetic Semiconductors*, edited by O. Madelung, Landolt-Börnstein, New Series, Group III Vol. 22 (Springer, Berlin, 1986); *Semiconductors:*

- Physics of II-IV and I-VII Compounds, Semimagnetic Semiconductors*, edited by O. Madelung, Landolt-Börnstein, New Series, Group III Vol. 17 (Springer, Berlin, 1982).
- ⁴⁴E. Menéndez-Proupin, C. Trallero-Giner, and A. Garcia-Cristobal, *Phys. Rev. B* **60**, 5513 (1999).
- ⁴⁵E. Menéndez, C. Trallero-Giner, and M. Cardona, *Phys. Status Solidi B* **199**, 81 (1997).
- ⁴⁶This value was estimated from neutron scattering spectroscopy and the rigid ion model from W. Szuszkiewicz, K. Dybko, E. Dynowska, J. Gorecka, B. Witkowska, and B. Hennion in *Proceedings of the 23rd International Conference on the Physics of Semiconductors*, edited by M. Scheffler and R. Zimmermann (World Scientific, Singapore, 1996), p. 253.
- ⁴⁷These values correspond to bulk material for CdS, CdSe, and HgS where the internal strain, S , is not taken into account. In the case of CdS/HgS the lattice constants differ by only 0.6% and the effects of the internal interface strain can be neglected. Nevertheless, for the CdSe/CdS structure the mismatch is near 3.6% and the ω_L and ω_T values at $P=0$ for both components should be shifted in comparison with those of the bulk parameters. Also, an estimation of the dielectric constants, ϵ_0 and ϵ_∞ , under strain follows from the Lyddane-Sachs-Teller relation. Since β_L and β_T are responsible for the quadratic curvature of the LO and TO phonon branches, these higher order parameters can be considered independent of S . In the calculations shown in Figs. 1–4 we assume that the strain effect of the host matrix on the structure is also negligible.
- ⁴⁸P. H. Borchers, G. F. Alfrey, D. H. Saunderson, and A. D. B. Woods, *J. Phys. C* **8**, 2022 (1975); R. Trommer, H. Muller, M. Cardona, and P. Vogl, *Phys. Rev. B* **21**, 4869 (1980); G. Irmer, M. Wenzel, and J. Moneche, *Phys. Status Solidi B* **195**, 85 (1996); S. Q. Wang and H. Q. Ye, *J. Phys.: Condens. Matter* **17**, 4475 (2005).
- ⁴⁹F. S. Manciu, R. E. Tallman, B. D. McCombe, B. A. Weinstein, D. W. Lucey, Y. Sahoo, and P. N. Prasad, *Physica E* **26**, 14 (2005).
- ⁵⁰A. A. Guzelian, J. E. B. Catari, A. V. Kadavanich, U. Banin, K. Hamad, E. Juban, R. H. Wolters, C. C. Arnold, and J. R. Heath, *J. Phys. Chem.* **100**, 7212 (1996).
- ⁵¹A. G. Rolo and M. I. Vasilevskiy, *J. Raman Spectrosc.* **38**, 618 (2007).
- ⁵²A. G. Rolo, M. I. Vasilevskiy, M. Hamma, and C. Trallero-Giner, *Phys. Rev. B* **78**, 081304(R) (2008).
- ⁵³H. Lange, M. Machón, M. Artemyev, U. Woggon, and Ch. Thomsen, *Phys. Status Solidi (RRL)* **1**, 274 (2007).
- ⁵⁴M. I. Vasilevskiy, A. G. Rolo, N. P. Gaponik, D. V. Talapin, A. L. Rogach, and M. J. M. Gomesa, *Physica B* **316-317**, 452 (2002).
- ⁵⁵B. B. Owen and S. R. Brinkley, *Phys. Rev.* **64**, 32 (1943).
- ⁵⁶InP and CdS have nearly matched lattice constants and bulk moduli, differing by only 0.7% and 3%, respectively (Ref. 43). The maximum shift in ω_L and ω_T due to the ambient internal biaxial strain is estimated to be $\sim 1 \text{ cm}^{-1}$ (i.e., $<0.3\%$) with smaller relative changes expected for the other (derivative) parameters in Table III. See, B. Jusserand and M. Cardona, in *Light Scattering in Solids V*, edited by M. Cardona and G. Guntherodt (Springer-Verlag, Berlin, 1989), pp. 124–128, ω_L $\omega_T \sim 1 \text{ cm}^{-1} <0.3\%$.
- ⁵⁷F. S. Manciu, Ph.D. dissertation, SUNY at Buffalo, 2004.
- ⁵⁸The use of pyridine or 4:1 methanol:ethanol media is not found to strongly affect the observed spectral features or their pressure dependence, as expected in media with no optical transitions near the phonon frequencies of interest.